V European Conference on Computational Fluid Dynamics
ECCOMAS CFD 2010
J. C. F. Pereira and A. Sequeira (Eds)
Lisbon, Portugal,14-17 June 2010

DYNAMIC CHARACTERIZATION OF AN ACTUATED BLUFF BODY WAKE

Gregor Gilka*, Dirk M. Luchtenburg*, Frank Thiele* and Marek Morzyński†

*Berlin Institute of Technology, Department of Fluid Dynamics and Engineering Acoustics,
Müller-Breslau-Str. 8, 10623 Berlin, Germany
e-mail: gregor.gilka@tu-berlin.de
†Poznan University of Technology, Institute of Combustion Engines and Transportation
Piotrowo 3, 60-965 Poznan, Poland

Key words: fluid dynamics, pod, dmd, low dimensional model, bluff body

Abstract. *The natural and periodically forced flow around a two-dimensional bluff body with a blunt rear end are numerically investigated using an unsteady Reynolds-averaged Navier-Stokes (URANS) calculation. The applied zero-net-mass-flux forcing at the rear end corners of the body leads to a drag reduction due to a significantly higher pressure at the stern of the body. The velocity field snapshots of the natural and actuated flow are analyzed by the proper orthogonal decomposition (POD) and the dynamic mode decomposition (DMD). This analysis provides insight in the effectuated changes by actuation, which can be used to develop dynamical models for active closed-loop flow control.*

1 INTRODUCTION

The flow around a D-shaped bluff body can serve as a benchmark problem for more complicated geometries like automobiles, ships etc. This flow is dominated by a geometry induced separation and can be characterized as a 'wake flow'. The separated flow is accompanied by a large pressure loss at the stern of the body. The negative effect of the pressure induced drag has been tried to reduce by several means. Examples include passive devices like: turbulators, riblets, splitter plates, but also active flow control solutions: base bleed, rotary oscillations, synthetic jets etc. [1] . A detailed study of the effectiveness of small size tabs for drag reduction is provided by Park *et al.* [7] . Modern flow control solutions typically include feedback, i.e. observations are used to provide feedback about the 'success' of the control and update the controller accordingly. An example is the phase control described in reference [8] , which desynchronizes the shear-layer dynamics, leading to postponed vortex formation and hence a drag reduction.

The objective of the current study is to gain more insight in the physical mechanism that causes drag reduction when phase control [8] is applied to the wake of a D-shaped body. To this end, the natural and actuated flow around the bluff body is simulated using the unsteady Reynolds-averaged equation (URANS). The velocity field snapshots are subsequently analyzed by two methods: the proper orthogonal decomposition (POD [3]) and the dynamic mode decomposition (DMD [9,11]). The POD method extracts coherent structures (mode) of the flow which are optimal and ordered with respect to their kinetic energy, whereas the DMD method retains modes which follow from a linear system ansatz and contain a fixed growth rate and frequency. Both methods provide physical insight into the actuation mechanism. In particular, the snapshot analysis shows how the energy is (re)distributed among the modes and which frequencies are predominant in the flow.

This paper is organized as follows. The configuration and its URANS simulation are described in § 2. This section also contains a discussion of the natural and periodically forced flow. Two methods for basis extraction, namely POD and DMD, are described in § 3. The corresponding analysis of the natural and actuated flow is described in § 3.3.1 and § 3.3.2 respectively. The main findings and their implications are summarized in § 4.

2 NUMERICAL SIMULATION

In this section, the configuration and setup of the bluff body are described. We also highlight some characteristics of the natural and actuated flow.

2.1 Configuration and setup

The flow around the two-dimensional bluff body is simulated with the fully implicit, pressure-based, structured, finite-volume code ELAN [14] . The flow solver is second order accurate in time and space. Convective fluxes are approximated by a higher order TVD-Scheme. The pressure is calculated with a SIMPLE-based algorithm with co-located storage arrangement using a generalized Rhie & Chow-Interpolation. The flow is simulated

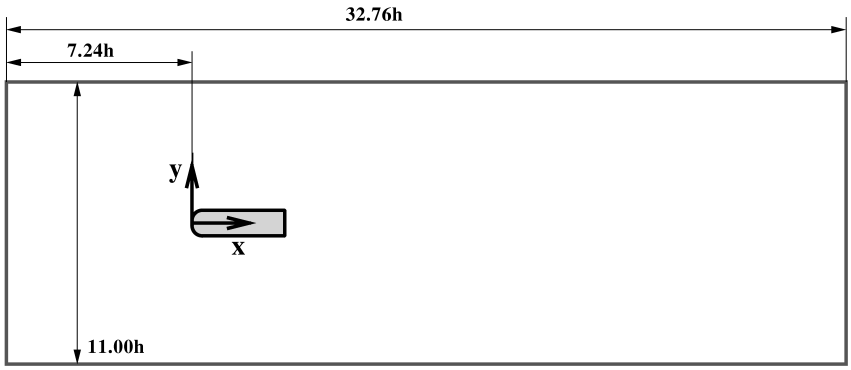

Figure 1: Setup of the configuration.

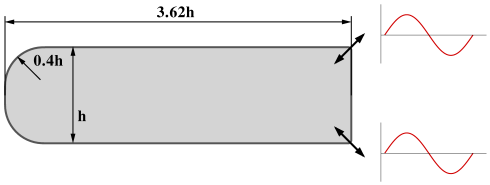

Figure 2: Dimensions of the bluff body and location of the actuators.

with the unsteady Reynolds averaged equations (URANS) using a standard k-ω-model by Wilcox [13] as closure model. The flow in the whole domain is treated fully turbulent.

For the simulation the bluff body is located in the center line of the computational domain, see figure 1. The Reynolds Number $Re = 30\,000$ is based on the height of the body h, the kinematic viscosity ν and the constant velocity u_∞ which are both fixed at the inlet of the domain. At the outlet a convective boundary condition is used. This allows an undisturbed downstream transport of the vortices descending from the stern of the body. At the wall of the bluff body a non-slip boundary condition is applied. The top and bottom boundary condition of the domain are prescribed by a symmetry or free-slip boundary condition. This mimics a blockage effect which is present in the wind tunnel experiments [8] and excludes boundary layer instabilities. The flow actuation is modelled by a time-dependent inflow boundary condition, which has been successfully applied in previous studies [10] .

The block-structured grid used in the CFD calculations is designed for a 2D URANS Simulation with $Re = 30\,000$. This includes a refinement of the grid near the wall of the bluff body to resolve the boundary layer with a low Reynolds boundary condition ($y^+ \leq 1$). An additional refinement in the wake region is introduced to resolve the large gradients. Using these conditions three different grids have been investigated. Table 1 shows the comparison of the grids with a different resolution but similar refinements. The wall-distance to the first grid point y^+ has not been modified. The mean value of the drag coefficient $\bar{c_D}$ and the value of nondimensional frequency St^n of the vortex shedding of the natural flow exhibit good convergence when the grid is refined. The medium grid is

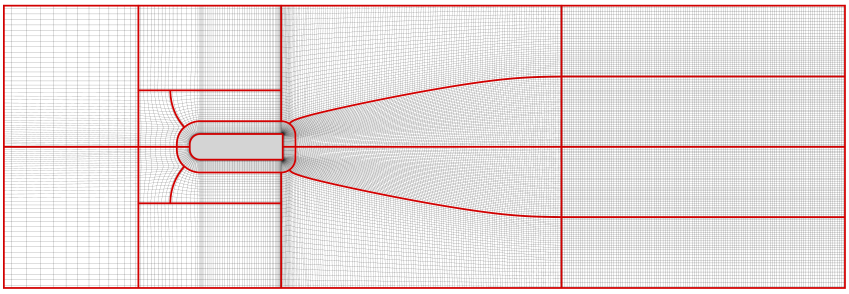

Figure 3: Overview of the investigated grid.

used for further calculations since this grid is a good compromise between accuracy and numerical effort.

grid	**number of elements**	$\mathbf{y^+}$	$\mathbf{\bar{c}_D}$	**St**
coarse	35 000	≤ 1	1.45	0.2695
medium	45 000	≤ 1	1.41	0.2659
fine	180 000	≤ 1	1.39	0.2617

Table 1: Comparison of different grid resolutions.

2.2 natural flow

The natural flow of the bluff body at $Re = 30\,000$ is dominated by unsteady vortex shedding, see figure 7. Figure 4 shows the time-dependent lift and drag coefficients of the body. The frequency of the lift is half the frequency of the drag due to the different influence of vortex shedding to the force on the body. The nondimensional frequency of vortex shedding is given by the Strouhal number:

$$St = \frac{f \cdot h}{u_\infty} \tag{1}$$

Figure 5 shows the power spectral density of the lift and drag coefficients. There are three dominant distinct frequencies which are listed with their values in table 2. The most dominant frequency has a value $St^n \approx 0.2659$ and corresponds to the vortex shedding of the natural flow. The second value is the Strouhal number of the drag coefficient which is two times larger than the latter. The last dominant frequency is given by $St \approx 0.7986$, which is three times larger than the vortex shedding frequency.

Besides these effects in the wake of the body two small recirculation areas are located directly behind the nose at the top and bottom of the body. Due to the high curvature of the nose the flow detaches and directly reattaches to the body after about $0.17h$ in flow direction. This behaviour has been observed in other studies [8] . The mean drag coefficient of the natural flow is $c_D = 1.412$.

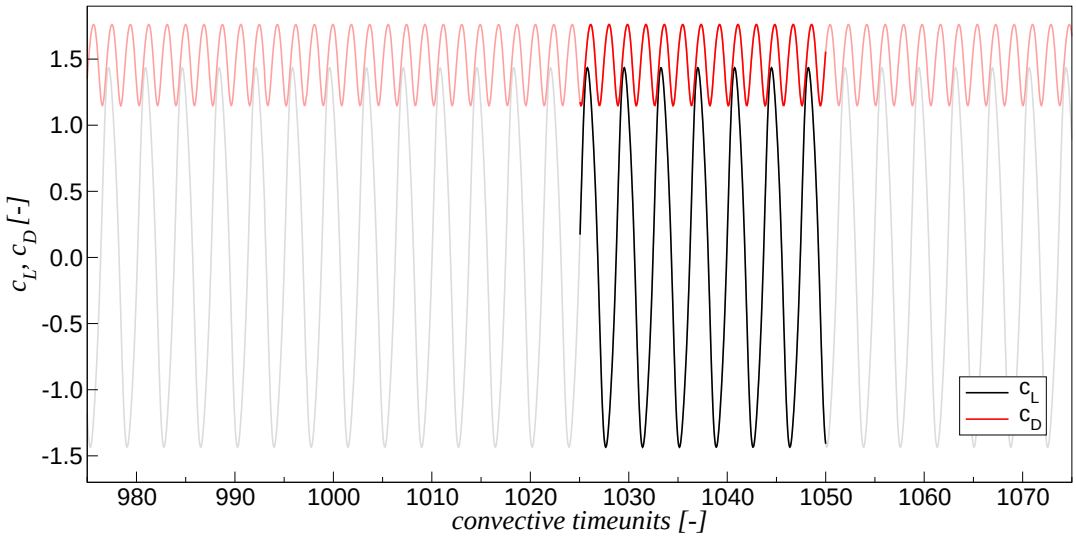

Figure 4: Lift and drag coefficient of the natural flow.

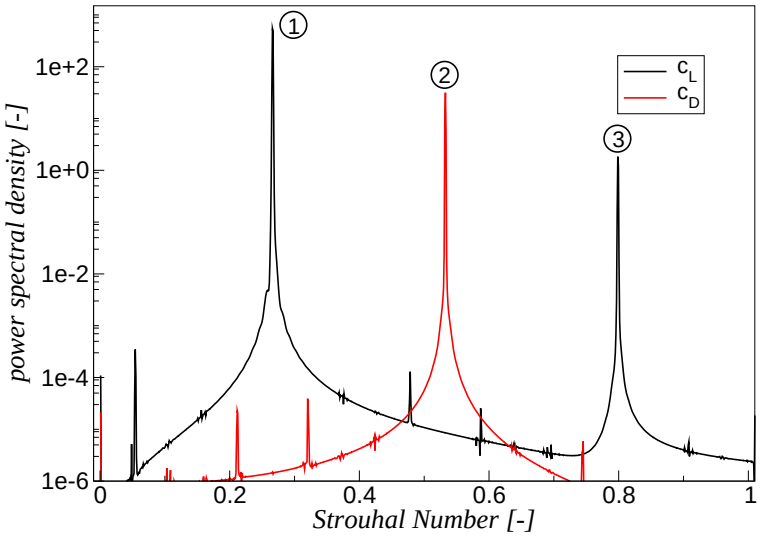

Figure 5: Power spectral density of lift and drag coefficient of the natural flow.

peak	**St** [-]	**psd** [-]
①	0.26589150	539.182160
②	0.53273601	31.476588
③	0.79862750	1.830190

Table 2: Strouhal numbers corresponding to the dominant frequencies of the natural flow.

2.3 Actuated flow

A harmonic zero-net-mass-flux actuation is applied to the flow at the corners at the stern of the body, see figure 2. The spatial distribution of the velocity at the inlet of the actuation slot is a block profile and its time-varying amplitude is set according to:

$$u_{act}(t) = u_{act,max} \cdot \sin(\omega t) \tag{2}$$

where $u_{act,max}$ is the maximum velocity, $\omega = 2\pi f$ the circular frequency and t is the simulation time. The nondimensional impulse coefficient c_μ quantifies the impulse of the actuation compared to the impulse of the undisturbed flow:

$$c_\mu = 2 \cdot \frac{s}{h} \frac{u_{act,max}}{u_\infty^2} \tag{3}$$

where s is the width of the actuation slot. The leading 2 refers to the two actuation slots which operate in phase. Their amplitude of actuation is chosen such that $c_\mu = 0.009$. The Strouhal number of the actuation is set to $St^a = 0.17$. These parameters were used in previous studies [8] .

Figure 8 shows the power spectral density of the lift and drag coefficients of the actuated flow. The actuators introduce additional frequencies with respect to the natural flow. This is exemplified by figure 9 which shows the power spectral density of the actuated flow. The Strouhal number of the vortex shedding of the natural flow is still present (compare table 3). The power spectral density of this frequency has been reduced to about 63%. The second most dominant frequency is the actuation frequency $St^a \approx 0.17$. This frequency can only be observed in the drag coefficient of the body due to the symmetry of the in-phase actuation. The lift coefficient is not effected. The third and fourth most dominant frequencies are the sum and the difference of the natural and actuation

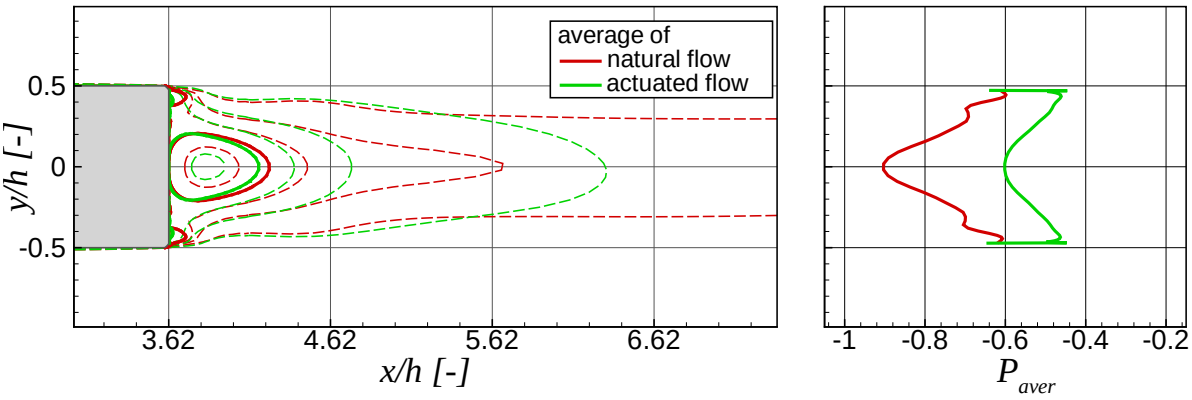

(a) Horizontal u-velocity iso-lines of the time-averaged flow field. The zero-line is highlighted to indicate the recirculation region.

(b) Average pressure at the stern of the body.

Figure 6: Comparison of the averages of the natural and the actuated flow.

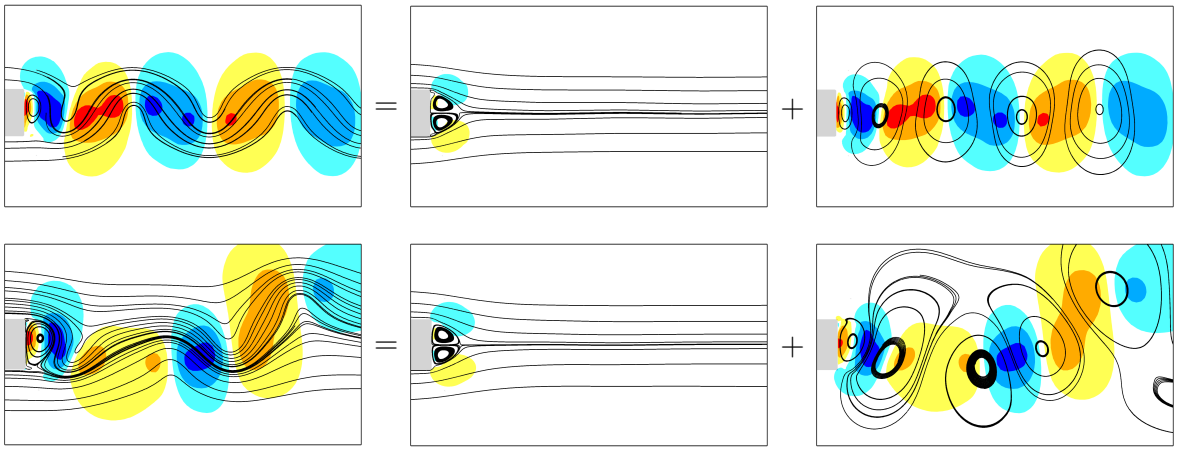

Figure 7: Reynolds decomposition of a snapshot of the natural (top row) and actuated (bottom row) flow field. The lines are streamlines and colors indicate the v-velocity.

Strouhal numbers. These additional frequencies appear due to the superposition of the natural vortex shedding frequency and the actuation frequency.

The mean drag coefficient of the actuated flow is $c_D = 0.996$. This corresponds to a drag reduction of about 30%. The reason for this drag reduction lies in a higher pressure at the stern of the body. Figure 6(b) shows the spatial pressure distribution of the time-averaged flow at the stern of the body. In each vertical position the pressure of the actuated flow lies between 0.1-0.3$[Pa]$ over the pressure of the natural flow. Together with the reduced length of the recirculation area (compare figure 6(a)) behind the body this implies the reduction of the time-averaged drag coefficient.

The Reynolds decomposition of a charateristic snapshot is shown in figure 7.

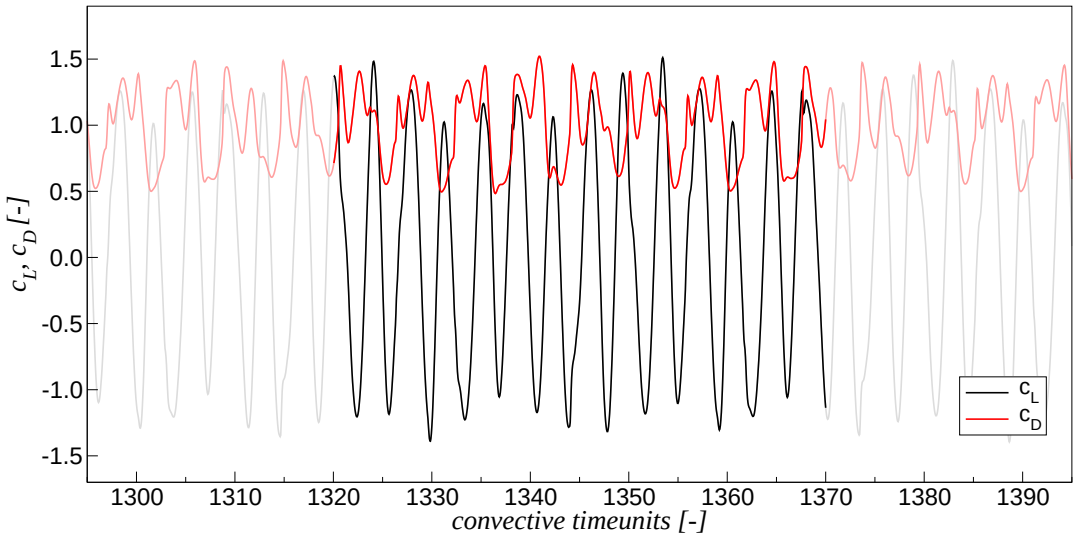

Figure 8: Lift and drag coefficient of the actuated flow.

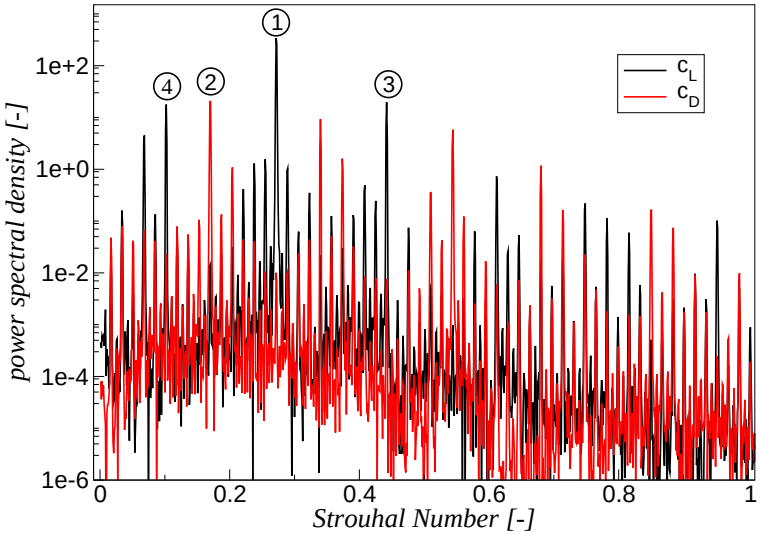

Figure 9: Power spectral density of lift and drag coefficient of the actuated flow.

peak	St [-]	psd [-]
①	0.27157895	342.504680
②	0.17052632	20.275385
③	0.44210526	19.739277
④	0.10210526	17.784728

Table 3: Strouhal numbers of the dominant frequencies of the actuated flow.

3 LOW-DIMENSIONAL MODELING

In this section, a low-dimensional representation is developed for the natural and actuated flow around the bluff body. The velocity field snapshots are approximated by a low-dimensional basis:

$$\mathbf{u}(\mathbf{x},t) = \mathbf{u}_0(\mathbf{x}) + \sum_{i=1}^{N} a_i(t)\,\mathbf{u}_i(\mathbf{x}), \tag{4}$$

where $\mathbf{u}_0$ is the time-averaged flow, a_i a temporal amplitude and $\mathbf{u}_i$ a spatial mode, and N denotes the number of retained modes. In the following, two methods of base extraction are considered: the "proper orthogonal decomposition" (POD), see § 3.1, and the "dynamic mode decomposition" (DMD), see § 3.2.

3.1 Proper Orthogonal Decomposition

The POD method extracts modes from an ensemble of snapshots which are sorted with respect to their kinetic energy content. The method is thoroughly described elsewhere [3,2] , and only its main properties are recaptulated. Premise for the POD is spatial correlation (coherence) of the velocity flow field. The optimal (POD) modes $\mathbf{u}_i$ are defined as the eigenfunctions of the Fredholm equation

$$\int_\Omega \mathbf{R}(\mathbf{x},\mathbf{y})\mathbf{u}_i(\mathbf{y})\,d\mathbf{y} = \lambda_i \mathbf{u}_i(\mathbf{x}), \tag{5}$$

where $\mathbf{R}(\mathbf{x},\mathbf{y})$ is the two-point autocorrelation tensor for the flow field, defined by

$$\mathbf{R}(\mathbf{x},\mathbf{y}) = \overline{\mathbf{u}(\mathbf{x},t) \otimes \mathbf{u}(\mathbf{y},t)}. \tag{6}$$

Here the overbar denotes time-averaging. The modes are ordered with respect to the decreasing real positive eigenvalues $\lambda_1 \geq \lambda_2 \geq \ldots \geq \lambda_N \geq 0$. The kinetic energy contained in mode i is measured by the eigenvalue λ_i, and the sum of the eigenvalues is equal to the total energy in the snapshots. Using the orthonormality of the modes, the time-dependent amplitudes follow from the projection

$$a_i(t) = (\mathbf{u}(\mathbf{x},t), \mathbf{u}_i(\mathbf{x}))_\Omega, \tag{7}$$

where the inner product is defined by an integral over the computational domain Ω: $(\mathbf{a},\mathbf{b})_\Omega = \int_\Omega \mathbf{a}\cdot\mathbf{b}\,d\mathbf{x}$. The method of snapshots developed by Sirovich [12] is used to compute the POD.

3.2 Dynamic Mode Decomposition

The dynamic mode decomposition (DMD) provides, like POD, a basis for a snapshot ensemble. It provides an alternative to POD if an ensemble of *time-resolved* snapshots is available. The evolution of the snapshots is assumed to be governed by a linear dynamic

system. As in linear stability analysis, the eigenvalues of the state matrix characterize the frequencies and the growth rates of the system. Hence, DMD can be viewed as a Laplace analysis of the snapshots. For a detailed description of the method, the reader is referred to references [9,11] .

Let an ensemble of M snapshots be given and stack the first $M-1$ snapshots in a matrix $\mathbf{X} = \{\mathbf{u}_1, \ldots, \mathbf{u}_{M-1}\}$, where $\mathbf{u}_k \in \mathbb{R}^N$. The basic premise of the method is that the snapshots are assumed to be generated by a linear dynamical system:

$$\mathbf{u}_{k+1} = \mathbf{A}\mathbf{u}_k. \tag{8}$$

The eigenvalues and eigenvectors of the matrix $\mathbf{A}$ completely characterize the behaviour of the dynamical system. The DMD is a method to compute the approximate eigenvectors or Ritz vectors of the system matrix. The Ritz vectors are called the Koopman or dynamic modes. Assume that the last snapshot in the ensemble can be expressed as a linear combination of the previous snapshots, i.e.

$$\mathbf{u}_M = \mathbf{A}\mathbf{u}_{M-1} = c_1\mathbf{u}_1 + \ldots + c_{M-1}\mathbf{u}_{M-1} = \mathbf{X}\mathbf{c}, \tag{9}$$

where $\mathbf{c} = (c_1, \ldots, c_{M-1})$. In general, this equality is not satisfied and instead $\mathbf{c}$ is computed as the least square approximation. The snapshots are related by the following matrix equation

$$\mathbf{A}\mathbf{X} = \mathbf{X}\mathbf{C}, \tag{10}$$

where $\mathbf{C}$ is a companion matrix

$$\mathbf{C} = \begin{bmatrix} 0 & 0 & \ldots & 0 & c_1 \\ 1 & 0 & & 0 & c_2 \\ 0 & 1 & & 0 & c_3 \\ \vdots & & \ddots & & \vdots \\ 0 & \ldots & 0 & 1 & c_{M-1} \end{bmatrix}. \tag{11}$$

The eigenvalues and eigenvectors of $\mathbf{C}$, given by $\mathbf{C}\mathbf{a} = \lambda\mathbf{a}$, directly lead to (a subset of) the eigenvalues and eigenvectors of $\mathbf{A}$. The spectral decomposition of $\mathbf{C}$ can be written as

$$\mathbf{C} = \mathbf{T}^{-1}\mathbf{\Lambda}\mathbf{T}, \tag{12}$$

where the eigenvectors are columns of $\mathbf{T}^{-1}$ and $\mathbf{\Lambda} = \mathrm{diag}(\lambda_1, \ldots, \lambda_{M-1})$. Using this notation, the Koopman modes are given by the columns of the following matrix

$$\mathbf{V} = \mathbf{X}\mathbf{T}^{-1}. \tag{13}$$

This leads to the connection between the snapshot matrix and the modal decomposition: $\mathbf{X} = \mathbf{V}\mathbf{T}$, where $\mathbf{T}$ contains the temporal amplitudes.

The growth or decay rate of a mode is usually used as a selector to extract unstable or stable modes.

3.3 Results

In this section, the velocity field snapshots of the natural and actuated flow are analyzed with the POD and DMD method.

3.3.1 Characterization of the natural flow

The natural flow is characterized by vortex shedding with a Strouhal number of 0.27, which is predominant in the lift coefficient, see figure 5, and also in the flow field. For the POD method, the flow field is Reynolds decomposed in its time-average and fluctuation part. The fluctuation part of the velocity field is decomposed with the POD method. The eigenvalues in figure 10 represent the energy in the POD modes. This spectrum reveals a dominant mode pair, which captures about 95% of the fluctuation energy, which is typical of vortex shedding. The first six modes and their amplitudes are shown in figures 11 and 12 respectively. The temporal amplitudes of the first mode pair $\{\mathbf{u}_1, \mathbf{u}_2\}$ indeed reveal a Strouhal number of 0.27. The second and third POD mode pair are associated with higher harmonics of relative low energy.

A dynamic mode decomposition of the natural flow almost resembles the results obtained by the POD analysis. The flow field is highly periodic and the coherent structures appear as (almost) pure harmonics. The first DMD mode corresponds to the time-averaged flow and consecutive DMD modes appear as complex-conjugate pairs. The first complex-conjugate pair of DMD modes resolves the vortex shedding at $St^n = 0.27$. The real and imaginary part of the second DMD mode are shown in figure 13 and closely resemble the first two POD modes. A slight advantage of the DMD method is that the temporal amplitudes by definition contain a single frequency, which is not the case for the amplitudes of the POD modes (see figure 12 (b), (c)).

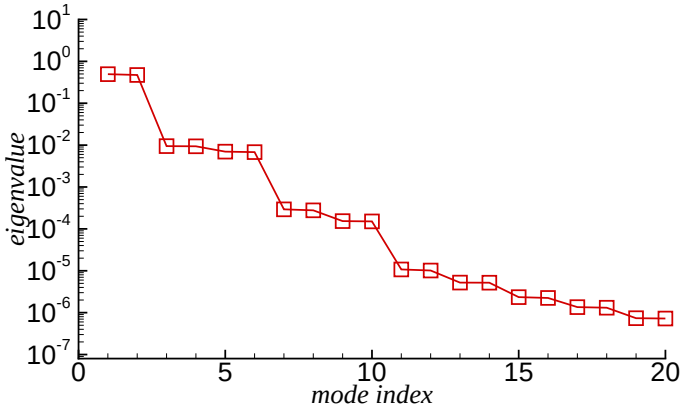

Figure 10: POD spectrum of the natural flow for the first 20 modes.

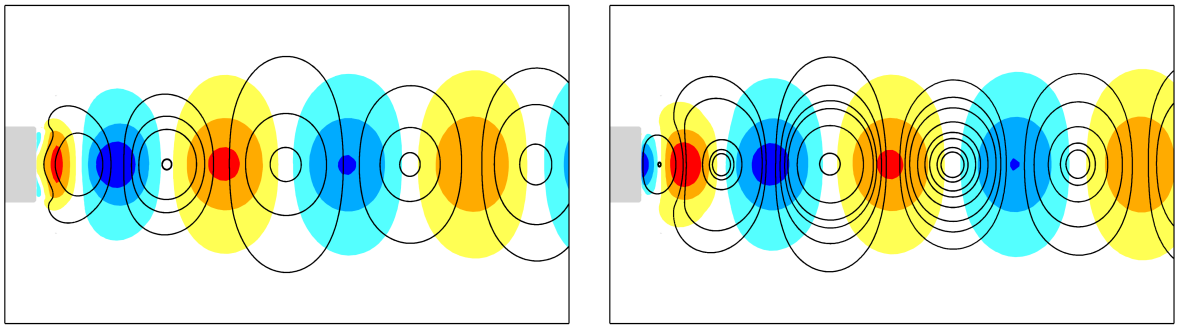

(a) $\mathbf{u}_1(\mathbf{x})$ (b) $\mathbf{u}_2(\mathbf{x})$

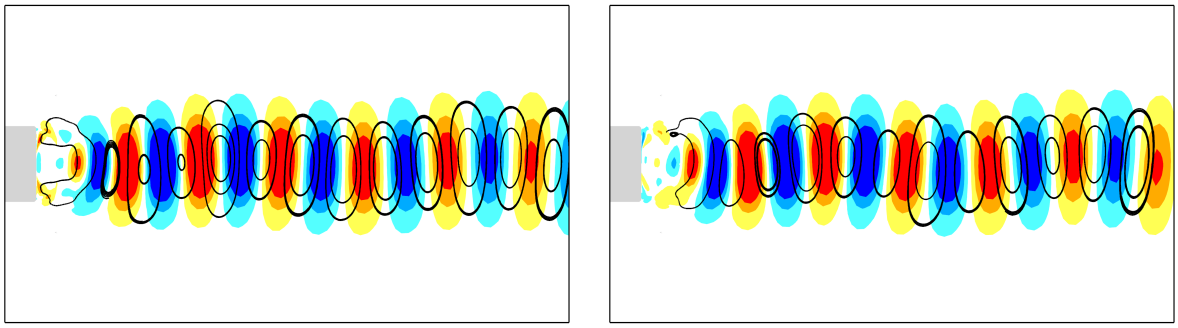

(c) $\mathbf{u}_3(\mathbf{x})$ (d) $\mathbf{u}_4(\mathbf{x})$

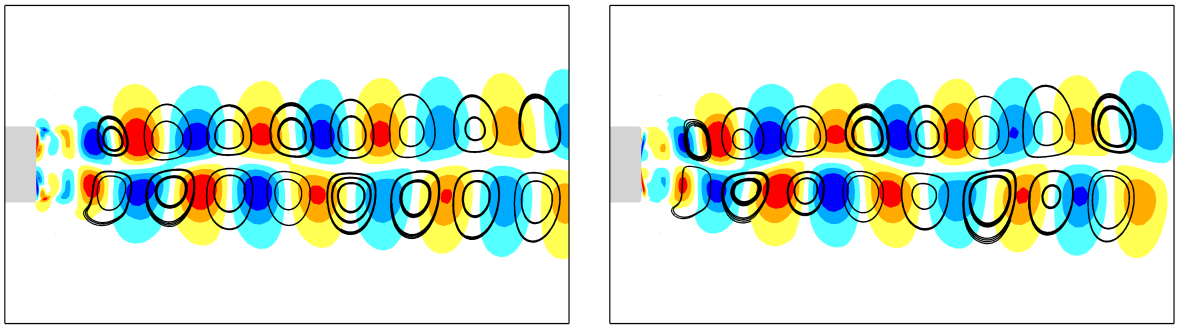

(e) $\mathbf{u}_5(\mathbf{x})$ (f) $\mathbf{u}_6(\mathbf{x})$

Figure 11: POD modes of the natural flow. The v-velocity (red: positive, blue: negative) and the stream lines are shown.

3.3.2 Characterization of the actuated flow

The actuated flow is dominated by two frequencies: the natural shedding frequency at $St^n = 0.27$ and the actuation frequency $St^a = 0.17$. Note that the natural and actuation frequency are not harmonically related. The interplay of these two leads to the beating frequencies $0.27 - 0.17 = 0.1$ and $0.27 + 0.17 = 0.44$, see figure 9 and table 3. The POD spectrum also reveals, see figure 14, two dominant mode pairs, which correspond to the natural and actuation frequency respectively. These first four modes contain 50% of the total kinetic energy. The following mode pair (mode 5 and 6) contributes less

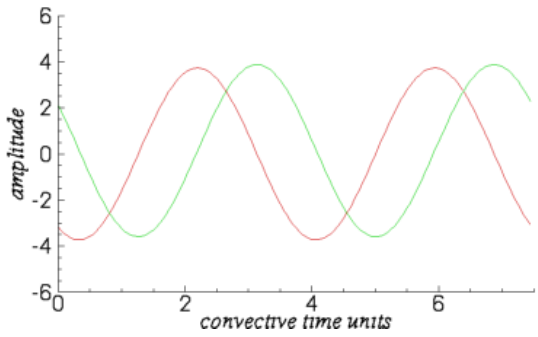

(a) $a_1(t)$, $a_2(t)$

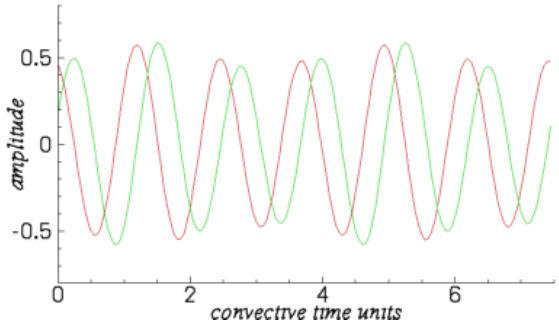

(b) $a_3(t)$, $a_4(t)$

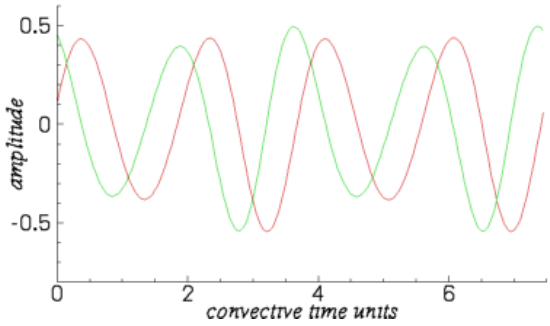

(c) $a_5(t)$, $a_6(t)$

Figure 12: The temporal amplitudes $a_i(t)$ corresponding to the POD modes in figure 11.

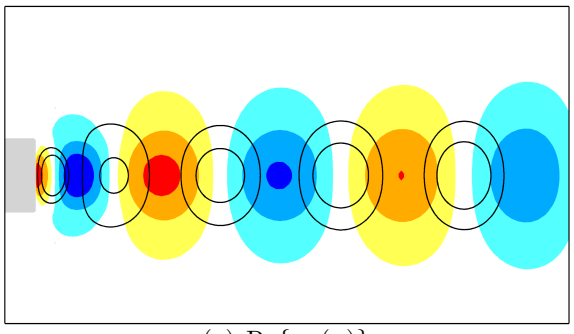

(a) $\mathrm{Re}\{\mathbf{u}_2(\mathbf{x})\}$

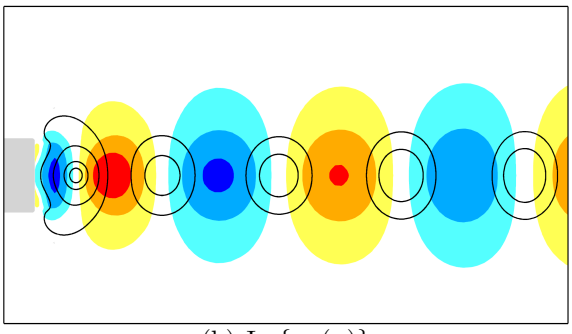

(b) $\mathrm{Im}\{\mathbf{u}_2(\mathbf{x})\}$

Figure 13: DMD modes (real and imaginary parts) of the natural flow. The v-velocity (red: positive, blue: negative) and the stream lines are shown.

than 2% to the total energy. This implies that energy is redistributed among the mean flow (compare figure 6) and higher order modes. The POD does not clearly separate the coherent structures that correspond to the natural flow frequency and the actuation frequency. This is illustrated in figure 15 where the temporal amplitudes of the first POD mode and the corresponding DMD mode are compared. In figure 16, in the left column from top to bottom, the real parts of the DMD modes are shown that correspond to

the frequencies in table 3. For comparison the POD modes that are most similar to the DMD modes are shown in the right column of the figure. The clear structures revealed by the DMD analysis are evident when compared to POD. A sorting algorithm based on the time-averaged squared amplitudes of the normalized DMD modes shows that table 3 indeed reveals an order for the dominant flow structures which are sorted with respect to frequency and energy content.

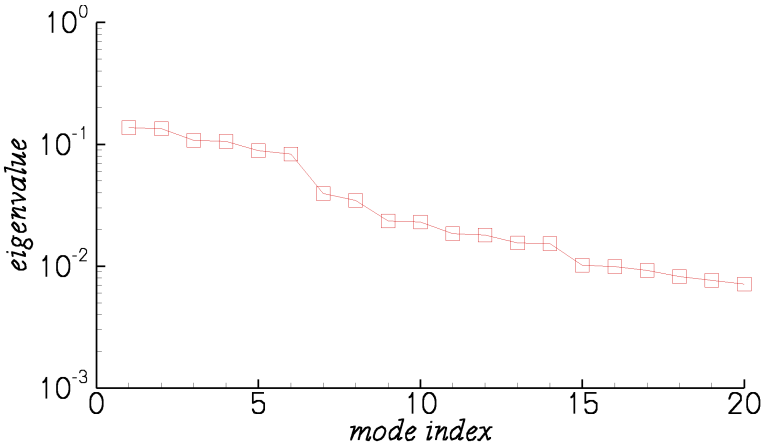

Figure 14: POD spectrum of the actuated flow for the first 20 modes.

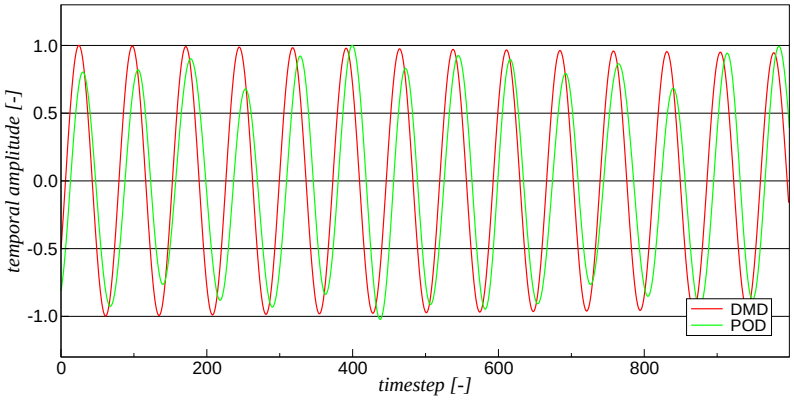

Figure 15: Comparison of the first POD and corresponding DMD mode amplitude of the actuated flow.

4 CONCLUSION

The natural and periodically forced flow around a two-dimensional bluff body was investigated using an URANS simulation. The actuation changes the mean flow dramatically and leads to an increased base pressure and hence reduces drag. The velocity field snapshots were analyzed with the POD and DMD method. The analysis reveals that the natural flow is dominated by vortex shedding. Analysis of the actuated flow shows that

the the coherent structures of the natural are still present, although the zero-net-mass-flux actuation at about 60% of the natural shedding frequency introduces new structures which are locked-in on this frequency. The interplay of the natural and actuation frequency leads to beating frequencies which are calculated as the superposition and the difference of both. These effects are most important since other modes have neglible energy content.

As described above, the actuators introduce new coherent structures that lock-in on the actuation frequency. These structures are believed to change the mean flow positively via the Reynolds stress. This assumption is corroborated by the fact that the natural and actuated oscillations are not harmonically related by integral or half-integral ratios. These observations will be pursued in the future to derive a Galerkin system, which is inspired by the dynamics of the system [4] .

References

[1] H. Choi, W.P. Jeon & J. Kim, Control of flow over a bluff body, *Annu. Rev. Fluid Mech.*, **Vol 40**, pp. 113–139. (2008).

[2] L. Cordier & M. Bergmann, Proper orthogonal decomposition: An overview. Tech. rep., Von Kármán Institute for Fluid Dynamics, (1999).

[3] P. Holmes, J.L. Lumley & G. Berkooz, *Turbulence, Coherent Structures, Dynamical Systems and Symmetry*, Cambridge University Press., (1998).

[4] D.M. Luchtenburg, B. Günther, B.R. Noack, R. King, G. & Tadmor, A generalized mean-field model of the natural and high-frequency actuated flow around a high-lift configuration, *J. Fluid Mech.*, **Vol 623**, pp. 283–316. (2009).

[5] B.R. Noack, K. Afanasiev, M. Morzyński, G. Tadmor & F. Thiele, A hierarchy of low-dimensional models for the transient and post-transient cylinder wake, *J. Fluid Mech.*, **Vol 497**, pp. 335–363. (2003).

[6] B.R. Noack, P. Papas & P.A. Monkewitz, The need for a pressure-term representation in empirical Galerkin models of incompressible shear flows, *J. Fluid Mech.*, **Vol 523**, pp. 339–365. (2005).

[7] H. Park, D. Lee, W.P. Jeon, S. Hahn, J. Kim, J. Choi & H. Choi, Drag reduction in flow over a two-dimensional bluff body with a blunt trailing edge using a new passive device, *J. Fluid Mech.*, **Vol 563**, pp. 389–414 (2006).

[8] M. Pastoor, et al., Feedback shear layer control for bluff body drag reduction, *J. Fluid Mech.*, **Vol. 608**, pp. 161–196 (2008).

[9] C.W. Rowley, I. Mezić, S. Bagheri, P. Schlatter & D.S. Henningson, Spectral analysis of nonlinear flows, *J. Fluid Mech.*, **Vol 641**, pp. 115–127 (2009).

[10] M. Schatz, B. Günther and F. Thiele, Computational Investigation of Separation Control for High-Lift Airfoil Flows, *Active Flow Control, Notes on Numerical Fluid Mechanics and Multidisciplinary Design*, **Vol. 95**, pp. 173–189 Springer (2007).

[11] P.J. Schmid, Dynamic mode decomposition of numerical and experimental data, *J. Fluid Mech., in Press*, (2010).

[12] L. Sirovich, Turbulence and the dynamics of coherent structures. part 1 : Coherent structures, *Quarterly of Applied Mathematics*, **Vol 45**, pp. 561–571 (1987).

[13] D.C. Wilcox, Reassessment of the scale determining equation for advanced turbulence models, *AIAA Journal*, **Vol. 26**, pp. 1299–1310 (1988).

[14] L. Xue, Entwicklung eines effizienten parallelen Lösungsalgorithmus zur dreidimensionalen Simulation komplexer turbulenter Strömungen, PhD thesis, *Technische Universität Berlin* (1998).

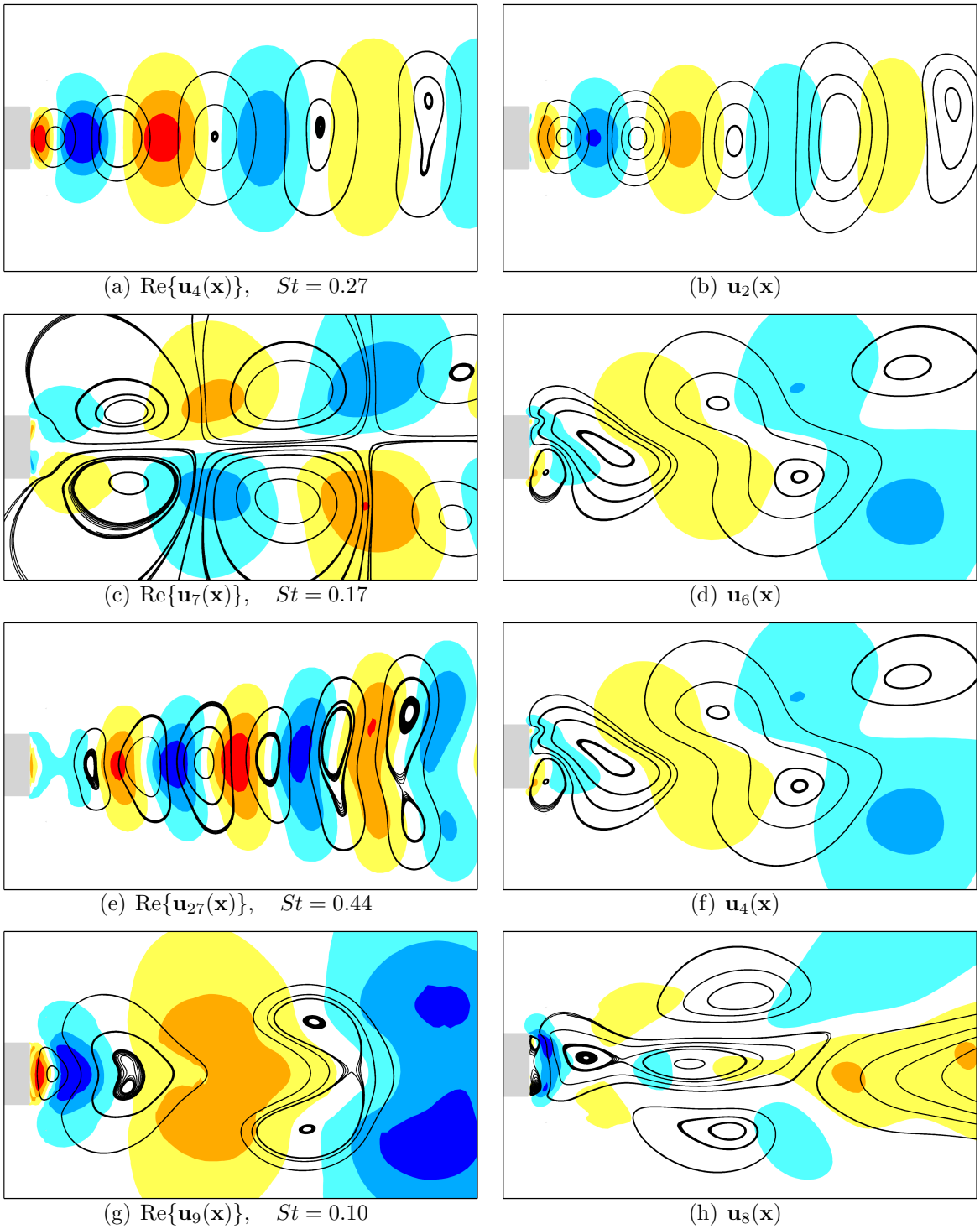

(a) $\mathrm{Re}\{\mathbf{u}_4(\mathbf{x})\}$, $St = 0.27$ (b) $\mathbf{u}_2(\mathbf{x})$

(c) $\mathrm{Re}\{\mathbf{u}_7(\mathbf{x})\}$, $St = 0.17$ (d) $\mathbf{u}_6(\mathbf{x})$

(e) $\mathrm{Re}\{\mathbf{u}_{27}(\mathbf{x})\}$, $St = 0.44$ (f) $\mathbf{u}_4(\mathbf{x})$

(g) $\mathrm{Re}\{\mathbf{u}_9(\mathbf{x})\}$, $St = 0.10$ (h) $\mathbf{u}_8(\mathbf{x})$

Figure 16: Comparison of the DMD modes (left) and POD modes (right) real parts of the actuated flow. The v-velocity (red: positive, blue: negative) and the stream lines are shown.